Machine learning based aerosol and ocean color joint retrieval algorithm for multiangle polarimeters over coastal waters

KAMAL ARYAL,[1] PENG-WANG ZHAI,[1,*] MENG GAO,[2,3] BRYAN A. FRANZ,[3] KIRK KNOBELSPIESSE,[3] AND YONGXIANG HU[4]

[1]*Department of Physics, University of Maryland Baltimore County, 1000 Hilltop Circle, Baltimore, MD 21250, USA*
[2]*Science Systems and Applications, Inc., Lanham, MD, 20706, USA*
[3]*NASA Goddard Space Flight Center, Code 616, Greenbelt, MD 20771, USA*
[4]*MS 475, NASA Langley Research Center, Hampton, VA 23681-2199, USA*
[*]*pwzhai@umbc.edu*

Abstract: NASA's Plankton, Aerosol, Cloud, ocean Ecosystem (PACE) mission, recently launched in February 2024, carries two multiangle polarimeters (MAPs): the UMBC Hyper-Angular Rainbow Polarimeter (HARP2) and SRON Spectropolarimeter for Planetary Exploration One (SPEXone). Measurements from these MAPs will greatly advance ocean ecosystem and aerosol studies as their measurements contain rich information on microphysical properties of aerosols and hydrosols. The Multi-Angular Polarimetric Ocean coLor (MAPOL) joint retrieval algorithm has been developed to retrieve aerosol and ocean color information, which uses a vector radiative transfer (RT) model as the forward model. The RT model is computationally expensive, which makes processing a large amount of data challenging. FastMAPOL was developed to expedite retrieval using neural networks to replace the RT forward models. As a prototype study, FastMAPOL was initially limited to open ocean applications where the ocean Inherent Optical Properties (IOPs) were parameterized in terms of one parameter: chlorophyll-a concentration (Chla). In this study we further expand the FastMAPOL joint retrieval algorithm to incorporate NN based forward models for coastal waters, which use multi-parameter bio-optical models. In addition, aerosols are represented by six components, i.e., fine mode non absorbing insoluble (FNAI), brown carbon (BrC), black carbon (BC), fine mode non absorbing soluble (FNAS), sea salt (SS) and non-spherical dust (Dust). Sea salt and dust are coarse mode aerosols, while the other components are in the fine mode. The sizes and spectral refractive indices are fixed for each aerosol component, while their abundances are retrievable. The multi-parameter bio-optical model and aerosol components are chosen to represent the coastal marine environment. The retrieval algorithm is applied to synthetic measurements in three different configurations of MAPs in the PACE mission: HARP2 observations only, SPEXone observations only and combined HARP2 and SPEXone observations. The retrieval results from synthetic measurements show that for aerosol retrieval the SPEXone-only configuration works equally well with the HAPR2-only configuration. On the other hand, for ocean color retrieval the SPEXone instrument provides better information due to its larger spectral coverage. For the surface parameters (wind speed), HARP2 measurements provide better information due to its wide field of view. Combined measurement configuration HARP2+SPEXone performed the best to retrieve all aerosol, ocean color and surface parameters. We also studied the impact of sun glint to aerosol and ocean color retrievals. The retrieval test revealed that wind speed and absorbing aerosol retrieval improves significantly when including measurements at glint geometries. Furthermore, the retrieval algorithm is equipped with modules for atmospheric correction and bidirectional reflectance distribution (BRDF) correction to obtain the remote sensing reflectance, which enables ocean biogeochemistry studies using the PACE polarimeter data.

1. Introduction

Satellite observation of global ocean color plays a key role in understanding ocean ecology and biogeochemistry [1–3]. It provides valuable information for the estimation of phytoplankton biomass [4], primary productivity [5–7], and dissolved [8] and particulate carbon [9], which advances the knowledge of the carbon cycle and helps quantify its impact on climate change. It is also a great avenue to obtain the information about atmospheric aerosols, which sheds light on the aerosol impacts on various aspects from human health to climate radiative forcing [10, 11].

Recent advances in satellite remote sensing observations include multi- angle polarimeters (MAPs), such as POLarization and Directionality of the Earth's Reflectance (POLDER) [12], Airborne Multiangle SpectroPolarimetric Imager (AirMSPI) [13], the airborne Spectro-polarimeter for Planetary EXploration (SPEX airborne) [14], Research scanning polarimeter (RSP) [15], the airborne Hyper Angular Rainbow Polarimeter (AirHARP), and HARP cubesat [16]. They have offered unique opportunities along with challenges in retrieving aerosol and ocean color information. On the one hand, MAP measurements contain rich information on microphysical properties of aerosols and hydrosols that makes it possible to obtain aerosol and ocean properties over complex coastal environments. On the other hand, processing a huge volume of data acquired from these sensors requires complex and efficient joint retrieval algorithms and large computational resources [17, 18].

A new development is NASA's Plankton, Aerosol, Cloud, ocean Ecosystem (PACE) mission, recently launched in February 2024, which carries two polarimeters: University of Maryland Baltimore County (UMBC) HARP2 [19] and Netherlands Institute for Space Research (SRON) SPEXone [20, 21]. HARP2 is a wide field-of-viewing sensor that measures polarized radiances at 4 wavelengths (440, 550, 670, and 865 nm) with different numbers of viewing angles (10 at 440, 550, and 865 nm, and 60 at 670 nm). SPEXone is a narrow swath imaging sensor which measures linearly polarized radiance at 5 viewing angles in a continuous spectral range from ultraviolet (UV) to near infrared (385–770 nm).

Several joint retrieval algorithms [22–26] have been developed to retrieve aerosol and ocean color information from MAP measurements, which use a bio-optical model parameterized by a single parameter chlorophyll-a (Chla). These algorithms are suitable for open ocean cases where the ocean water inherent optical properties (IOP's) covary with chlorophyll concentration, though their use is not appropriate over coastal waters, or even open ocean waters that vary from the ideal [27]. [28] developed a joint retrieval algorithm called Multi-Angular Polarimetric Ocean color (MAPOL) which uses a generalized seven parameter bio-optical model suitable for coastal waters. The joint retrieval algorithms typically perform iterative optimization by calling vector radiative transfer (RT) models on-the-fly as the forward model. The RT simulation is computationally expensive, which makes it challenging in the operational processing of MAP measurements.

Several works have been reported to increase the efficiency of joint retrieval algorithms, which use neural networks to replace RT based forward models. [29] demonstrated that a retrieval algorithm with NN based forward models called FastMAPOL is accurate and efficient to process data from HARP like instruments for both synthetic and airborne field campaign data [30, 31]. [32] introduced a retrieval scheme with cascaded neural networks to further optimize retrieval speed. [33] used a NN based forward model trained on combined HARP2 and SPEXone wavelengths. Both [29, 32] and [33] presented retrieval results using a bio-optical model parameterized by a single parameter Chla.

Aerosols over coastal waters are composed of a complex mix of particles from natural sources of both continental and marine origin (eg. dust and sea salt) and anthropogenic processes (eg. black carbon, brown carbon and water-soluble aerosols) emitted from urban and industrial activities. Some of these aerosol components (eg. brown carbon and dust) have a strong spectral signature with increased absorption towards blue and UV wavelengths. Aerosol models based on flexible microphysical properties can represent such spectral signatures by using the principal components of refractive index spectra along with size variables as free parameters [28]. Another way is to use the aerosol component approach, where aerosols are assumed to be a mixture of volume fractions of different components with fixed size distribution and refractive index spectra. In such approach, volume fractions of aerosols become the free parameters. Recently, the component approach has been implemented in GRASP (Generalized Retrieval of Aerosol and Surface Properties) algorithm [34, 35]. The GRASP component approach has also been shown to improve the retrieval of aerosol optical properties (especially very low bias in AOD) compared to aerosol models parameterized by microphysical properties [34, 35]. The component approach also results in a smaller retrieval parameter space which helps to improve stability of retrieval algorithms.

In this work, we propose a joint retrieval algorithm called FastMAPOL/component which evolves from FastMAPOL but uses a multi parameter bio-optical ocean model and component representation of aerosols which are suitable for coastal waters. The aerosol components are chosen to represent typical marine atmosphere in coastal regions which encompass a wide range of spectral refractive indices and sizes. The retrieval algorithm is augmented by the modules for atmospheric correction and Bidirectional Reflectance Distribution Function (BRDF) correction to obtain remote sensing reflectance from MAP measurements.

The two polarimeters (HARP2 and SPEXone) in the PACE mission provide different measurement capabilities. HARP2 has a wider swath, whereas the spectral range and sampling of SPEXone is larger. Synergistic measurements from both polarimeters offer a unique opportunity to decipher the signals from different constituents of aerosol and ocean bodies [17]. It is vital to have a thorough information content analysis on the retrievability of different aerosol and ocean color properties with these measurements [17, 18, 36]. For example, [37] discussed the trade-off between spectral sampling and the number of viewing angles for MAP instruments, and found that the aerosol retrieval accuracy is slightly increased when the number of viewing angles is increased from three at the cost of the number of spectral sampling points. Similar results have been shown for aerosol retrieval from RSP [38], AirMSPI [39], and HARP instruments [30]. For the retrieval of ocean parameters UV wavelengths and more spectral coverage in blue-green range can be equally important. In order to facilitate such exploration, the FastMAPOL/component retrieval algorithm is designed to be capable of using measurements from three different configurations of MAPs in PACE mission: HARP2-only (H), SPEXone-only (S) and HARP2+SPEXone (H+S). We studied the performance of the aerosol and ocean parameter retrievals from different configurations. In addition, we have also studied the impact of sun glint to the retrieval of different parameters. The glint measurements have been shown to be effective in the retrieval of wind speed and absorbing aerosols which are usually present over coastal waters [36, 40].

This paper is organized as follows: section 2.3 defines the materials and methods used in this work, section 3 presents the results and discussion, section 4 summarizes the conclusion reached from this study.

2. Materials and methods

This section covers the framework of the FastMAPOL/component retrieval algorithm. We will first describe the component representation of aerosols used in the retrieval algorithm in Sec. 2.1, then cover the bio-optical model of coastal ocean waters in Sec. 2.2. Several neural network models will be trained to act as the forward model for the least squares fitting process. A radiative transfer model based on the successive orders of scattering method (RTSOS) [41, 42] is used to generate a synthetic training dataset for neural networks. In Sec. 2.3, we describe the RTSOS settings including the wavelengths selection and the ranges of input parameters for the radiative transfer simulations of coupled atmosphere and ocean systems. The radiation quantities generated by the radiative transfer model is covered in Sec. 2.4. The neural network training process is described in Sec. 2.5. FastMAPOL/component retrieval algorithm is presented in Sec. 2.6.

2.1. Component representation of Aerosol

In the FastMAPOL/component algorithm aerosols are represented by an external mixture of different components with assumed size distribution and refractive index spectra. The components are resolved in two size modes: fine mode and coarse mode. The fine mode aerosols consist of fine mode non-absorbing insoluble (FNAI), brown carbon (BrC), black carbon (BC) and fine mode non absorbing soluble (FNAS), whereas the coarse mode consists of sea salt (SS) and non-spherical dust (Dust). These components represent the most abundant marine aerosols found in the coastal environment and align with the aerosol components in chemical transport models such as Global Ozone Chemistry Aerosol Radiation and Transport (GOCART) model [43]. The volume fraction of these components along with total aerosol loadings are treated as retrieved parameters, whereas their size and refractive index are fixed. The real and imaginary refractive index spectra of components are taken from published experimental data literature. They are plotted in figure 1 with their sources. Each aerosol component follows the lognormal size distribution:

$$\frac{dV_i\left(r\right)}{dlnr} = \frac{V_i}{\sigma_i\sqrt{2\pi}}\exp\left(-\frac{\left(lnr - lnr_i\right)^2}{2\sigma_i{}^2}\right) \tag{1}$$

Where, r_i and σ_i represent the respective dry radius by volume and the standard deviation of a component with total volume column density V_i. The dry radius by volume (r_i) and standard deviation (σ_i) of different components are taken from the references as summarized in table 1.

The components FNAI, BC and Dust are hydrophobic whereas SS and FNAS are hygroscopic and their growth factors are taken from Optical Properties of Aerosol and Clouds (OPAC) package [44]. 50% of BrC are assumed to be hygroscopic, the rest being hydrophobic similar to organic carbon component of GOCART. The growth factors at different relative humidities are used in the single parameter growth equation from [45] to obtain the parameter (γ) as,

$$\frac{r_{RH}}{r_\circ} = \left(\frac{1}{1 - RH}\right)^{\frac{\gamma}{3}} \tag{2}$$

The parameter γ solved from $r_{RH}/r_\circ$ at known RH values can used to obtain the radius at any relative humidity (r_{RH}) from dry radius ($r_\circ$).

Polarimetric single scattering properties of spherical components are modeled using the Lorenz-Mie code developed by [46]. The non-spherical dust properties are adopted from [47]. The aerosol number density N as a function of height z is assumed to be gaussian with peak represented by aerosol layer height (ALH) [48].

$$N\left(z\right) = A\ exp\left(-4ln2\frac{\left(z - z_c\right)^2}{\sigma^2}\right) \tag{3}$$

where z_c is the aerosol layer height in km, A is a normalizing factor determined from total aerosol loading and microphysical parameters, and σ is the width of aerosol height distribution which is fixed at 2 km.

The aerosol retrieval parameters include total aerosol optical depth (AOD), aerosol layer height (ALH), fine mode fraction (FMF) and the volume fractions of four aerosol components (FNAI, BrC, BC, SS). The volume fractions of fine and coarse modes are normalized to one so that the volume fractions of FNAS and Dust are determined by FNAS=1-FNAI-BrC-BC and Dust=1-SS. The total volume fractions of each component are determined by multiplying them with FMF (fine mode) and 1-FMF (coarse mode), respectively. The overall aerosol phase matrix is a sum of the fine and coarse modes weighted by FMF. The retrieved fractions along with RH can be used in the single scattering calculation to obtain single scattering albedo (SSA) which is an important optical property of aerosols.

Table 1. Description of aerosol components and their parameters of lognormal size distribution

Component	Description	$(r_i(\mu m),\sigma_i)$
BC	Strongly absorbing component (wavelength independent) of biomass burning.	(0.05,0.444) [44]
BrC	Absorbing (both water soluble and insoluble) organic carbon with strong absorption towards UV wavelengths.	(0.14,0.444) [49]
FNAI	Non absorbing dust like component (dust and non absorbing insoluble organics in fine mode).	(0.16,0.444) [50]
FNAS	Non absorbing water soluble inorganic salts, secondary marine aerosols from oxidation of dimethyl sulfide (DMS) related compounds, can also represent non absorbing water soluble components of volcanic eruptions.	(0.31,0.444) [44]
SS	Coarse mode sea salts.	(2.9,0.672) [50, 51]
Dust	Non spherical mineral dust transported over marine atmosphere.	(3.0,0.693) [44, 52]

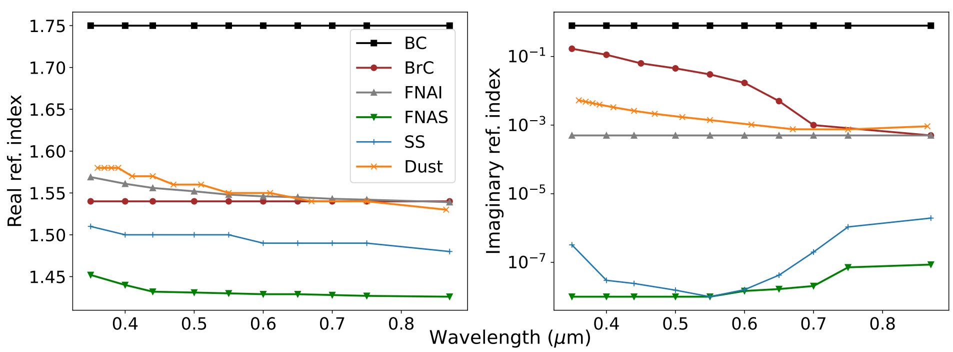

Fig. 1. Refractive index of aerosol components : BC [53], BrC [54], FNAI [44, 55], FNAS [44], SS [44] and Dust [52, 56].

2.2. Ocean bio optical model

Ocean waters are assumed to consist of four components: pure sea water, phytoplankton particles, non-algal particles (NAP) and colored dissolved organic matter (CDOM). The parameterizations of the IOPs are [28]:

$$a_{ph}(\lambda) = A_{ph}(\lambda)[Chla]^{E_{ph}(\lambda)} \tag{4}$$

$$a_{dg}(\lambda) = a_{dg}(440)exp[-0.018(\lambda - 440)] \tag{5}$$

$$b_{bp}(\lambda) = b_{bp}(660)\ [\lambda/660]^{-S_{bp}} \tag{6}$$

$$B_p(\lambda) = B_p \tag{7}$$

where the wavelength λ is in nm, a_{ph} denotes the absorption coefficient for phytoplankton particles, a_{dg} is the total absorption coefficient for both NAP and CDOM, b_{bp} and B_p are the total backscattering coefficient and total backscattering fraction for all particles (phytoplankton and NAP) respectively. Values of the coefficients A_{ph} and E_{ph} are obtained from [57]. S_{bp} is the polynomial spectral slope for $b_{bp}(\lambda)$. Spectral exponent factor for a_{dg} is fixed at 0.018 [58] and spectrally invariant B_p is used [59]. These spectral slopes were shown to work well in the inversion of insitu and satellite measurements [60, 61]. The absorption coefficient $a_w(\lambda)$ and scattering coefficient $b_w(\lambda)$ for pure sea water are taken from the experimental data [62–64]. The backscattering fraction for water is 0.5 [65]. The total absorption coefficient, backscattering coefficient and scattering coefficient can be calculated as follows:

$$a(\lambda) = a_w(\lambda) + a_{ph}(\lambda) + a_{dg}(\lambda) \tag{8}$$

$$b_b(\lambda) = b_{bw}(\lambda) + b_{bp} \tag{9}$$

$$b_p = b_{bp}/B_p \tag{10}$$

The scattering coefficient for CDOM is assumed to be negligible. All ocean parameters are assumed to be independent of ocean depth i.e parameters are assumed uniform throughout the water column. The ocean depth is fixed at 200m, and floor is assumed to be completely absorbing. Note that the contribution of radiation signal from the depth below 200m from the surface will be minimal at TOA. The Fourier-Forand (FF) phase function [66, 67] is used to represent the phase function of the ocean water particulate matter, which is determined by the backscattering fraction B_p [66]. The FF function agrees with various in-situ volume scattering function (VSF) measurements [68]. We adopt Voss and Fry's measurement of average ocean waters [69] to represent the Mueller matrix of ocean waters.

2.3. Data preparation

2.3.1. Selection of wavelength bands

HARP2 measures light intensity and polarization at 4 channels in the visible and near infrared (440, 550, 670, and 870 nm) whereas SPEXone measures intensity at hyperspectral bands and polarization at 50 channels ranging from UV to NIR. Out of 50 channels from SPEXone and HARP2 measurements, we selected 13 bands in the atmospheric windows, which are selected to be consistent with the wavelengths available in heritage ocean color sensors such as Moderate-Resolution Imaging Spectrometer (MODIS), Sea-viewing Wide Field-of-view Sensor (SeaWiFS) and Visible Infrared Imaging Radiometer Suite (VIIRS). We didn't use all available bands from SPEXone instrument mainly because the simulation of hyperspectral intensity and polarization requires a large amount of computational resources which makes it prohibitive in retrieval algorithms. In addition, the previous studies found that 15-17 discrete bands are sufficient for resolving most ocean color features based on an analysis of the in-situ measured remote sensing reflectance spectrum of different ocean water types [70, 71]. It may be favorable to adopt the O2 A (near 765 nm) and B bands (near 680 nm) to obtain aerosol vertical height distribution [72]. We will explore this possibility in the future.

2.3.2. Radiative transer simulation

The vector radiative transfer model based on the successive order of scattering method (RTSOS) [41, 42] is used for the simulation of synthetic dataset. RTSOS has been widely used in the development and validation of neural network algorithms for aerosol and ocean color remote sensing applications [29, 32, 73–75]. The inherent optical properties of aerosols, i.e., absorption and scattering optical depths, as well as the phase matrices, are mixed with those of the molecular atmosphere to obtain their total values. Gas absorption due to H_2O, CO_2, O_2, CH_4, ozone, and NO_2 are considered and their vertical profiles were taken from 1996 US standard atmosphere [76], though only ozone amount is allowed to vary in the synthetic dataset. The profile data includes the total number density of atmospheric molecules and the volume mixing ratios of the significant absorbers (H_2O, CO_2, O_2, CH_4, and NO_2) in the UV-SWIR spectral range. Note that the changes in their vertical profile due to change in temperature are insensitive to the measurements as the simulated channels are in the atmospheric windows. The surface pressure is set to 1013 hPa. This parameter will be treated as variable in the next version of retrieval algorithm as it may have impact on the Rayleigh signal in the UV wavelengths. Readers are referred to [77] for more details. An improved pseudo spherical shell (IPSS) correction algorithm is used to treat the spherical shell effects which improves the fidelity of simulations for larger solar and viewing zenith angles [78]. The ocean surface roughness is parameterized in terms of wind speed (W) [79] and foam reflectance is considered following [80]. Several internal parameters that determine the numerical accuracy of RTSOS simulations include the number of scattering orders (N_s), the number of Gaussian quadratures for discretizing the viewing zenith angle in the atmosphere (P_a) and ocean (P_o) and the order of Fourier decomposition (M) for the viewing azimuth angle. These parameters are fixed at N_s=40, P_a=80, P_o=120, M=20, which are sufficiently high to ensure the accuracy of radiative transfer calculation. For each solar zenith angle, the polarized reflectance was calculated for all viewing angles within the ranges with an angular resolution of 1°. The resulting range of scattering angle is (50 –180). For each case corresponding to a specific solar zenith angle, the simulated reflectance and DoLP is an array of shape (60,180). For the training of Neural networks, for each case we used reflectance and DoLP corresponding to 500 different random pairs of viewing zenith and azimuth angles (described in section 2.5).

A total of 24,500 cases covering a wide range of aerosol, surface and ocean parameters under various solar and viewing geometries were generated using RTSOS. The range of parameters is summarized in table 2. Random uniform distribution is used to sample all parameters except three ocean IOPs (Chla,$a_{dg}(440)$,$b_{bp}(660)$) which are sampled randomly using uniform distribution in logarithmic scale. For a given Chla, $a_{ph}(440)$ is calculated using equation 4, and other IOPs ($a_{dg}(440)$ and $b_{bp}(660)$) are generated randomly using constraints (eq. 11,12) to their values at 440 nm. S_{bp} is generated using the constraint (eq. 13) based on Chla. The scheme shown in Eqs. (11-13) is similar to the approaches in [81–83] to reproduce naturally found covariation among different parameters, though our bounds are more relaxed to ensure the statistical independence of IOPs. The scheme will eliminate some extremely unlikely combinations which is important to reduce the ambiguity in inverse problems [84].

$$0.01 \times a_{ph} \leq a_{dg} \leq 100 \times a_{ph} \tag{11}$$

$$0.001 \times (a_{ph} + a_{dg}) \leq b_{bp} \leq 0.5 \times (a_{ph} + a_{dg}) \tag{12}$$

$$-0.5 + \frac{1}{1+\sqrt{Chla}} \leq S_{bp} \leq -0.4 + \frac{7}{1+\sqrt{Chla}} \tag{13}$$

The boundaries of parameter have been selected based on typical scenario focusing the application on ocean color remote sensing. In current simulation the upper limit of AOD is fixed at 0.5 as the water leaving signal reaching TOA will be undetectable at very high AODs. However, to detect the aerosol plumes in rare events over ocean like smoke or dust plume, the upper limit of AOD will be increased to 1.5 in future versions. Also, the upper limit of windspeed is fixed at 10 ms^{-1} to minimize the foam and white caps reflection.

2.4. Radiometric quantities simulated by RTSOS

MAP instruments provide intensity and polarization measurements or the Stokes parameters (L_t, Q, and U) at the top of atmosphere at different viewing angles and wavelengths. The total reflectance (ρ_t), degree of linear polarization, DoLP (P_t), reflectance from the system containing only atmosphere and ocean surface (ρ_{a+s}), water leaving reflectance reaching the sensor (ρ_w) , BRDF correction factor and remote sensing reflectance are calculated as follows:

$$\rho_t = \frac{\pi L_t}{\mu_0 F_0} \tag{14}$$

Table 2. Range of geometry (solar zenith angle($\theta_\circ$),viewing zenith angle(θ_v), relative azimuth angle(ϕ_v)), environmental (O_3, RH), aerosol (AOD, ALH, FMF, SS, FNAI, BC, BrC), surface (W) and ocean (Chla,$a_{dg}(440)$,$b_{bp}(660)$,B_p,S_{bp}) parameters used in the simulation of synthetic dataset. RT simulations of all cases are performed at 13 different wavelengths ($\lambda(nm)$=(385,400,410,441,470,490,510,530,549,620,670,740,873)).

Parameters (Units)	Range	Parameters (Units)	Range
$\theta_\circ$ (Degrees)	0–70	O_3(Dobson unit)	150–450
θ_v(Degrees)	0–60	RH (%)	0.3–0.99
ϕ_v(Degrees)	0–180	AOD (550)(Unitless)	0–0.5
$Chla(mgm^{-3})$	0.01–30	ALH(Km)	0.1–10
$a_{dg}(440)(m^{-1})$	0.001–2.5	FMF(Unitless)	0.1–1
$b_{bp}(660)(m^{-1})$	0.0001–0.1	SS(Unitless)	0–0.99
B_p(Unitless)	0.005–0.05	FNAI(Unitless)	0–0.4
S_{bp}(Unitless)	0–2	BC(Unitless)	0–0.1
W(ms^{-1})	0.5–10	BrC(Unitless)	0–0.5

where F_0 is the extraterrestrial solar irradiance, μ_0 is the cosine of the solar zenith angle.

$$P_t = \frac{\sqrt{Q^2 + U^2}}{L_t} \tag{15}$$

The water leaving reflectance reaching the sensor can be obtained through atmospheric correction as,

$$\rho_w = \rho_t - \rho_{a+s} \tag{16}$$

The remote sensing reflectance can be obtained as,

$$R_{rs} = \frac{\rho_w}{\pi} \times TBRDF, \quad TBRDF = \frac{BRDF}{T_d t_u} \tag{17}$$

where TBRDF is the BRDF correction factor including transmittances, T_d is the downwelling irradiance transmittance for the solar irradiance from TOA to the surface, and t_u is the upwelling radiance transmittance for the water-leaving radiance from surface to TOA.

2.4.1. Direct approach to calculate BRDF correction factor

The BRDF correction factor is defined as the ratio of water leaving radiance at zenith sun and nadir viewing direction to its value at arbitrary solar and viewing geometry. Traditional approaches for BRDF factor calculation employ different intermediate factor calculations with different assumptions for wind speed and geometry [66, 85]. However, these approaches were mainly developed and validated using data from open ocean waters and the systematic investigation of BRDF correction in coastal waters remains a topic of active research [86]. Taking advantage of the full suite of RTSOS which can generate Stokes parameters for coupled atmosphere and ocean systems, we calculated BRDF correction directly without involving the calculation of intermediate factors. For that purpose, we simulated radiances just above the ocean surface in four different scenarios viz. total radiance at arbitrary viewing geometry ($L_{t,0^+}(\theta_0, \theta_v, \phi_v)$), total radiance at zenith sun and nadir viewing geometry ($L_{t,0^+}(0,0)$), atmospheric and surface radiance for arbitrary viewing geometry ($L_{a+s,0^+}(\theta_0, \theta_v, \phi_v)$) , atmospheric and surface radiance for zenith sun and nadir viewing geometry ($L_{a+s,0^+}(0,0)$). Then the BRDF correction factor can be calculated directly form the definition as,

$$BRDF = \frac{L_{t,0^+}(0,0) - L_{a+s,0^+}(0,0)}{L_{t,0^+}(\theta_0, \theta_v, \phi_v) - L_{a+s,0^+}(\theta_0, \theta_v, \phi_v)} \tag{18}$$

where the subscripts 0^+ indicate that the radiances are evaluated just above the ocean surface. This direct approach accounts for all factors that contribute to the angular distribution of water leaving signal leaving no place for errors involved in intermediate calculation and hence is a better alternative to traditional approaches.

2.5. Training NN forward models

Four different multilayer perceptron neural network models are designed to predict the total reflectance (ρ_t), degree of linear polarization (P_t), reflectance from the system containing atmosphere and ocean surface (ρ_{a+s}), and BRDF correction factor divided by transmitances (TBRDF) at 13 different wavelengths as listed in table 2. The NN models for ρ_t and P_t are trained to act as forward models in the retrieval optimization whereas the models for ρ_{a+s} and TBRDF were trained to perform atmospheric correction and BRDF correction to obtain remote sensing reflectance. The model input parameters for ρ_t, P_t, and TBRDF are all 18 parameters from table 2 whereas the model for ρ_{a+s} takes only 13 parameters related to geometry, environmental, aerosol, and surface (excluding 5 ocean parameters from table 2) as inputs. All neural networks output radiometric quantities at 13 wavelengths. Of the total 24.5K cases, 23.5K cases are used in the training process (70% used for training and 30% used for validation) and the remaining 1K cases are used as test dataset to check the performance of developed models. For each simulated case, measurements corresponding to 500 different random pairs of viewing zenith and viewing azimuth angles are generated for training process. This leads to 11.75 million sets of data cases for training and validation. The mean squared error (MSE) loss function is used in the training TBRDF model. The loss functions for ρ_t, ρ_{a+s}, P_t are defined by normalizing the fitting residuals by the measurement uncertainty analogous to the retrieval cost function (eq. 24) [32].

$$\chi^2{}_{\rho_t} = \frac{1}{N}\sum_i \frac{\left[\rho_t(i) - \rho_t^{NN}(x;i)\right]^2}{\sigma_\rho^2} \tag{19}$$

$$\chi^2{}_{\rho_{a+s}} = \frac{1}{N}\sum_i \frac{\left[\rho_{a+s}(i) - \rho_{a+s}^{NN}(x;i)\right]^2}{\sigma_{\rho_{a+s}}^2} \tag{20}$$

$$\chi^2{}_{P} = \frac{1}{N}\sum_i \frac{\left[P_t(i) - P_t^{NN}(x;i)\right]^2}{\sigma_P^2} \tag{21}$$

These loss functions are advantageous over the MSE loss function as MSE can be dominated by peaked measurements in the glint region. This modification makes the training process aware of the measurement uncertainty of the instruments [21, 87] therefore optimizes in a way more relevant to the retrieval's operation. We used uncertainty (σ) of 3% for ρ_t and ρ_{a+s}, and 0.005 for DoLP in the above training loss functions.

Several different architectures and combinations of hyper parameters (including learning rate and activation function) are tested and the best performing models are selected as listed in table 3 with associated uncertainties. To train NNs, we employed the following strategies which further optimized the training strategy discussed by [29, 74]:

- Input parameters for all models are scaled in the range of [0,1] using their minimum and maximum values from the training dataset.

- The output parameters for models ρ_t, ρ_{a+s}, P_t are left unscaled to accommodate training loss functions defined in equations 19-21, whereas for TBRDF model, outputs are normalized through the division by their standard deviation.

- The hidden layers for models ρ_t, ρ_{a+s}, P_t use LeakyReLu activation function whereas the hidden layers for TBRDF model use Hyperbolic Tangent (Tanh) activation function.

$$LeakyReLu(z) = max(0, z) + 0.01 \times min(0, z) \tag{22}$$

$$Tanh(z) = \frac{(e^z - e^{-z})}{(e^z + e^{-z})} \tag{23}$$

- Exponential decay learning rate schedule is used. Learning rate is reduced by a factor of 10 every 150 epochs. The initial learning rate of 0.001 is used

- The batch size of 1000 is used.

- The Adam optimization algorithm [88] with weight decay regularization [89] is used. The optimization algorithm minimizes the loss function to find the optimal values for weights and bias metrices [90].

- Early stopping technique is used to decrease model training time and prevent overfitting. The model training was stopped when the model performance does not improve for 20 epochs and the best weights and bias are restored.

Table 3. Architecture and uncertainity of NN forward model and RT simulations in terms of RMSE ,values inside parentheses are RMSE of percentage difference.

Quantities	ρ_t	P_t	ρ_{a+s}	TBRDF	$\sigma_{RT}(\rho_t)$	$\sigma_{RT}(P_t)$
Architecture	18×600×300× 150 × 13	18×600×300× 150 × 13	14×600×300× 150 × 13	18×300× 150 × 13	n/a	n/a
$\sigma_{NN}(385)$	0.0006(0.26)	0.0009	0.0004(0.15)	0.010	0.00012	0.0002
$\sigma_{NN}(400)$	0.0006(0.25)	0.0008	0.0003(0.15)	0.008	0.00012	0.0002
$\sigma_{NN}(410)$	0.0005(0.25)	0.0008	0.0003(0.14)	0.007	0.00012	0.0002
$\sigma_{NN}(441)$	0.0005 (0.27)	0.0008	0.0003 (0.14)	0.006	0.00012	0.0002
$\sigma_{NN}(470)$	0.0005(0.29)	0.0009	0.0003(0.15)	0.006	0.00012	0.0002
$\sigma_{NN}(490)$	0.0005(0.31)	0.0010	0.0003 (0.16)	0.006	0.00012	0.0002
$\sigma_{NN}(510)$	0.0005(0.33)	0.0009	0.0003(0.17)	0.006	0.00012	0.0002
$\sigma_{NN}(530)$	0.0005(0.36)	0.0009	0.0003(0.18)	0.006	0.00012	0.0002
$\sigma_{NN}(549)$	0.0006(0.38)	0.0010	0.0004(0.25)	0.005	0.00005	0.0002
$\sigma_{NN}(620)$	0.0005(0.37)	0.0010	0.0004(0.25)	0.005	0.00005	0.0005
$\sigma_{NN}(670)$	0.0005(0.37)	0.0011	0.0005(0.24)	0.005	0.00010	0.0005
$\sigma_{NN}(740)$	0.0005(0.41)	0.0012	0.0004(0.29)	0.005	0.00015	0.0007
$\sigma_{NN}(873)$	0.0006(0.57)	0.0016	0.0006(0.39)	0.004	0.00015	0.0007

2.6. Joint retrieval framework

The NN models for ρ_t and P_t are used as forward models in the FastMAPOL/component joint retrieval algorithm to optimize the χ^2 cost function which quantifies the difference between measurement and forward model prediction as [91].

$$\chi^2(\mathbf{x}) = \frac{1}{N}\sum_i \left(\frac{\left[\rho_t\ (i) - \rho_t^f\ (\mathbf{x}; i)\right]^2}{\sigma_\rho^2} + \frac{\left[P_t\ (i) - P_t^f\ (\mathbf{x}; i)\right]^2}{\sigma_P^2} \right) \tag{24}$$

where i denotes the quantities at different wavelength and viewing angles, N denotes the total number of measurements used in the retrieval. ρ_t^f and P_t^f are the total reflectance and DoLP computed from the neural network forward model with the state vector $\mathbf{x}$. $\rho_t(i)$ and $P_t(i)$ represent measurements of corresponding quantities from MAP instruments. σ_ρ and σ_P are the total uncertainties in the reflectance and DoLP used in the algorithm. The total uncertainties include calibration/measurement uncertainty of the instrument (σ_m), forward model uncertainty of RTSOS (σ_{RT}) and forward model uncertainty of neural network (σ_{NN}) as:

$$\sigma^2 = \sigma_m^2 + \sigma_{RT}^2 + \sigma_{NN}^2 \tag{25}$$

The reflectance measurement uncertainties of 3% for HARP2 and 2% for SPEXone and DoLP measurements uncertainty of 0.005 for HARP2 and 0.003 for SPEXone are used [21, 87]. The NN forward model and RT forward model uncertainties are listed in table 3. In equation 24, we use a diagonal error covariance matrix with diagonal elements equal to the total uncertainties. The measurement uncertainties are assumed to be uncorrelated as their correlation strength is not well quantified.This may lead to inaccurate representation of the algorithm performance in the true instrument measurements [92], which is a subject of future studies.

The state vector $\mathbf{x}$ is divided into five groups of parameters, namely, geometry, environmental, aerosol, surface and ocean parameters (as mentioned in table 2 caption) . The aerosol, surface and ocean parameters are retrieved directly whereas the geometry and environmental parameters are treated as known in synthetic data tests. When applying the algorithm to real MAP data, the geometry parameters will be obtained from the instrument whereas the environmental parameters will be obtained from NASA GMAO MERRA2 data [93].

We used subspace trust-region interior reflective optimization approach [94] to minimize the cost function by varying the state parameters $\mathbf{x}$. The Jacobian matrices, used to determine the direction to update the state parameter, are derived analytically from the NN forward model using automatic differentiation based on chain rule differentiation [95] as explained and implemented in [30]. Once the convergence is met, the state parameters $\mathbf{x}$ are reported. The optimized state parameters $\mathbf{x}$ are used as input to the neural networks for ρ_{a+s} and TBRDF to determine the atmospheric signal and BRDF correction factors which are then incorporated in equations 16-17 to obtain remote sensing reflectance. The logistic flow of joint retrieval framework is summarized in figure 2.

2.6.1. Retrieval configurations for different MAPs

FastMAPOL/component has three configurations: HARP2-only, SPEXone-only, HARP2+SPEXone. The specifications of these configurations are summarized as follows:

- HARP2-only configuration takes measurements from 4 HARP2 wavelengths: 441, 549, 670, 873 corresponding to respective 10, 10, 60, 10 viewing zenith angles of the HARP2 instrument.

- SPEXone-only configuration takes measurements from 12 wavelengths (excluding 873 nm) corresponding to 5 viewing angles of SPEXone instrument.

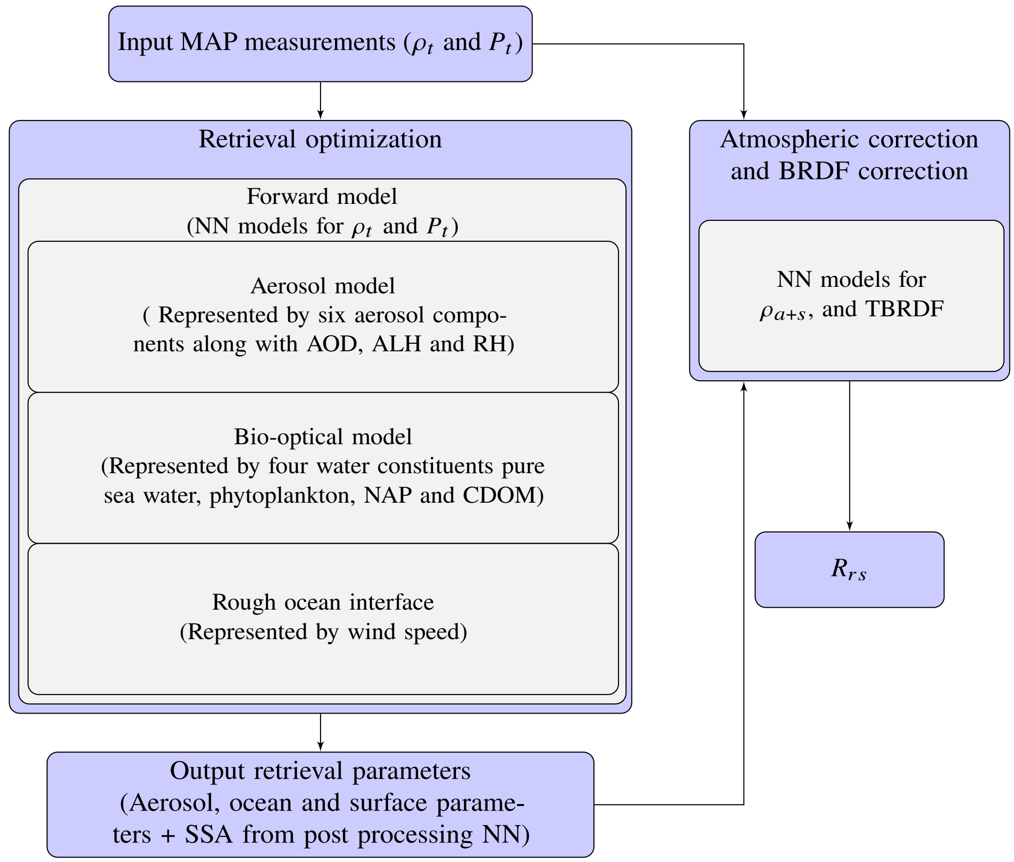

Fig. 2. Flowchart showing different components in the retrieval optimization of FastMAPOL/component.

- HARP2+SPEXone configuration takes measurements from all 13 wavelengths. The viewing angles at the 4 HARP2 wavelengths are taken following the HARP2 instrument and the remaining wavelengths following SPEXone.
- All configurations have two settings: one removing measurement from glint region (i.e. region with glint angle < 40) and other including those measurements.

The dimension of state vector ($\mathbf{x}$) is the same for all three combination which includes the aerosol (7 parameters), surface (1 parameter) and ocean parameters (5 parameters) with total 13 retrieval parameters in all combinations. As neural network forward models take normalized input parameters in the range [0-1], the first guess of all parameters is set to be 0.5.

3. Results and discussion

In section 3.1 we present the performance of the neural network forward model based on the test dataset. Section 3.2 covers the overall performance evaluation of FastMAPOL/component in terms of the cost function distribution and speed assessment, impact of glint measurements (section 3.2.1), retrievability evaluation of different retrieval configurations (section 3.2.2).

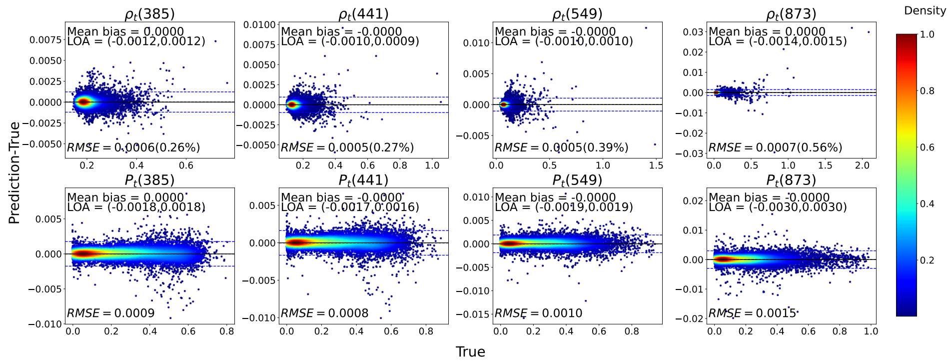

Fig. 3. NN forward models performance based on the test data for total reflectance (ρ_t, top row) and DoLP (P_t,bottom row) at selected wavelengths.

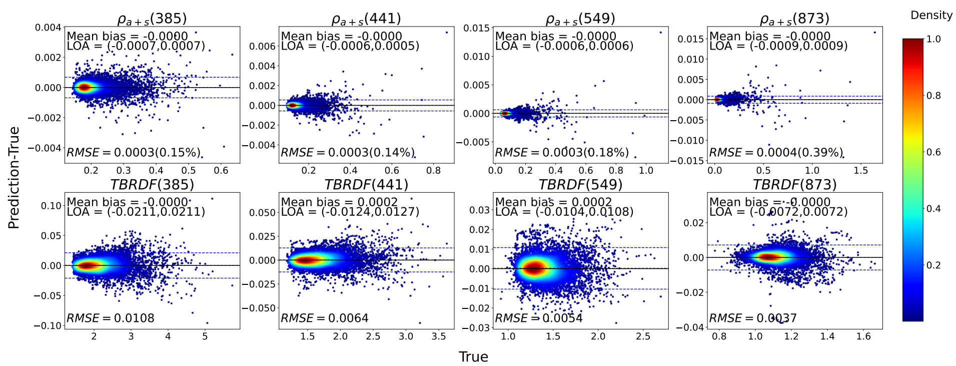

Fig. 4. NN forward models performance based on the test data for reflectance from atmosphere and surface(ρ_{a+s}, top row) and BRDF correction factor with transmittance(TBRDF,bottom row) at selected wavelengths.

3.1. Performance of NN forward models

The performance of trained NN models is evaluated with the test dataset containing 1K cases which were not used during the training process. For each case, corresponding quantities are calculated for 10 random pairs of viewing zenith and azimuth angles in the range mentioned in table 2. The measurements at glint viewing angles are also included in this performance evaluation. For the performance evaluation we used a difference plot also known as Bland Altmann (BA) plots [96], where the differences between prediction and true values are compared against their true values from RTSOS simulation. For each quantity, we calculate the mean bias and the limits of agreement (LOA) defined as 1.96 standard deviation around the mean bias. The mean bias value indicates any systematic bias in the model whereas the LOA represents 95% confidence intervals.

Figure 3 and 4 show NN models' performance at 4 selected wavelengths from 385 to 873 nm. The solid black line is the line of equality, the dashed black line indicates the mean bias, and the blue dashed lines show the limits of agreement (LOA). The color bar indicates the data point density normalized by its maximum value. Figure 3 top panel shows the NN model performance for total reflectance. The model predictions are highly accurate with zero mean bias at all wavelengths. The root mean squared error (RMSE) between predicted and true reflectance is less than 0.007 for all wavelengths. Percentage RMSE value increases from 0.26% for 385 nm to 0.56% for 873 nm as the magnitude of reflectance values at 873 nm are relatively small. This NN uncertainty is much lower compared to calibration uncertainty of 3% for HARP2 and 2% for SPEXone.

Figure 3 bottom panel shows the NN model performance for total DoLP. The model predicts DoLP at all wavelengths with zero mean bias. RMSE between predicted and true DoLP is less than 0.0015 for all wavelengths which is much lower than calibration uncertainty of 0.005 for HARP2 and 0.003 for SPEXone. As the errors show zero mean bias, RMSE is used as an proxy for one sigma uncertainty of NN forward models. These models have similar performance at other nine remaining wavelengths which is summarized in table 2 in terms of RMSE. These results confirm that the neural networks models are highly accurate with uncertainty much lower compared to measurement uncertainties and hence are suitable to be used as forward models in the joint retrieval algorithm.

Figure 4 top panel shows the NN model performance for reflectance from a system with only atmosphere and ocean surface (ρ_{a+s}). The model predicts ρ_{a+s} with zero mean bias and RMSE less than 0.0007 for all wavelengths and percentage RMSE increases from 0.15% at 385 nm to 0.4% at 873 nm. Figure 4 bottom panel shows the NN model performance to predict TBRDF. The RMSE value decreases from 0.01 at 385nm and to 0.0037 at 873 nm. TBRDF model shows a very small mean bias of 0.0002 at wavelengths 441 nm and 549 nm.

3.2. Performance of joint retrieval algorithm

The forward models for ρ_t and P_t are used to drive the joint retrieval algorithm to minimize the χ^2 cost function (eq. 24). We performed retrievals on 1K test cases which are generated by the RTSOS model. The test cases were not exposed to the NN models during the training process. The retrievals are performed for different measurement configuration viz. HARP2-only, SPEXone-only, and HARP2+SPEXone. In order to best represent the real data, random noise is added to the simulated reflectance and DoLP equal to measurement uncertainty of the instruments. The impact of including or removing measurements from the glint signal is also evaluated for all three configurations. Figure 5 left panel shows the distribution of χ^2 . The χ^2 distribution helps to test whether the noise model is realistic and how severe the local minimum convergence problem is, which exists in all non-linear squares fitting algorithms. χ^2 value close to 1 means that the average difference between the measurements and the forward models fitting is comparable to the total uncertainty. χ^2 much larger than 1 suggests suggests unreliable retrievals [91]. We chose retrievals with $\chi^2 < 1.5$ as good retrievals.

From figure 5, we can see that for H and H+S configuration, χ^2 distribution is centered around 1 in both situations of removing or including glint measurements indicating good fit. However, it is worth noting that for S configuration, when removing glint measurements, the χ^2 distribution is centered around 0.85 indicating slight over-fitting. This is due to the fact that the total number of available measurements may not be sufficient enough for all parameters causing overfitting of the model capturing the noise in the data. All χ^2 distribution is centered around 1 when the measurements from glint were included (left bottom).

Figure 5 right panel shows the distribution average times per retrieval for different configurations running on a single CPU core of Intel Xeon Gold 6140 Skylake processor. When the glint measurements are removed (top right), The S configuration is fastest taking around 0.15s on average per pixel whereas H+S takes around 0.23s. When the measurements in glint are included (bottom right), the average time per retrieval increased by approximately 50% for H+S, 33% for S and 25% for H configuration.

Considering the number of pixels in a single granule of HAPR2 measurements to be 395×519, the algorithm will take around 10.5 hours without glint measurements and 14 hours with glint

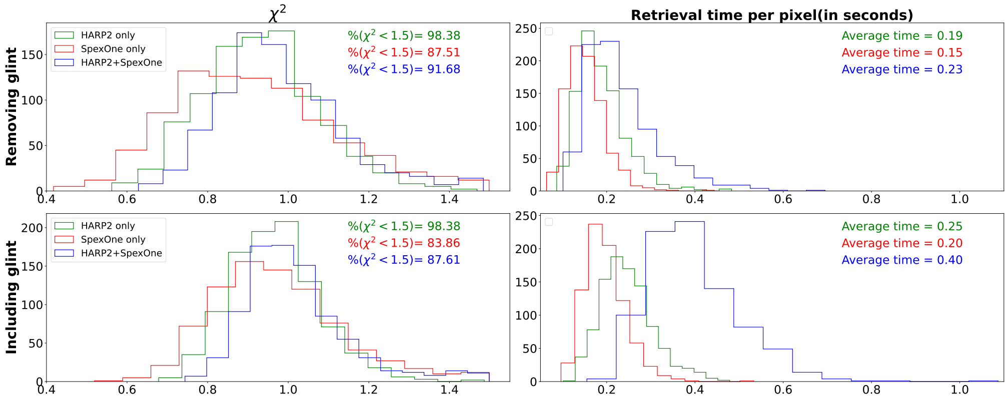

Fig. 5. Distribution of χ^2 and average retrieval time per pixel for different configurations

measurements to process one full HARP2 granule in a single CPU core. Similarly, to process single granule of SPEXone measurements (of size 395×29), it will take 5 hours without glint measurements and 6.5 hours with glint measurement in a single CPU core. A server with number of cores equal to the number of granules obtained in a day can be used to process the PACE polarimeter data operationally within the time taken for one granule. Even with the use of complex aerosol and ocean bio-optical models, FastMAPOL/component maintains comparable speed with FastMAPOL on HARP2 data which takes 0.2s/pixel and 0.1s/pixel respectively with and without implementing cascading NN [32].The speed also compares well with other widely used retrieval algorithms such as GRASP. To process the single pixel from POLDER/PARASOL measurement, it takes about 3-4s per pixel for GRASP/High Precision, 0.3-0.5s/pixel for GRASP/optimized and 0.1-0.2s/pixel for GRASP/Models [35]. However, it should be noted that the speed of algorithms may vary due to the different hardware, number of measurements and the precision used during the inversion.

All parameters from table 2, excluding geometry and environmental parameters, are retrieved directly from the FastMAPOL/component algorithm as explained in section 2.6. Two of the ocean parameters B_p, and S_{bp} were found to be less sensitive to the measurements resulting in higher error. We fixed them at 0.018 and 1 respectively following the existing practice in ocean color remote sensing where these parameters are either fixed [61, 97] or are derived afterwards from retrieved remote sensing reflectance [58, 98]. This contributed to slight improvements in the retrieval performance of other three ocean parameters.

The directly retrieved aerosol fractions (FMF, SS, FNAI, BC, BrC) and relative humidity were used as input to another neural network to predict single scattering albedo (SSA) at 550 nm. This neural network has two hidden layers with 64 neurons each with LeakyRelu activation and follows similar training strategy as that of TBRDF model. The NN model for SSA performs well in the test dataset with zero mean bias and RMSE of 0.0005 indicating that the model accurately represents the single scattering calculations as explained in section 2.1. Now, we discuss the performance of the joint retrieval algorithm under all 3 configuration settings both while removing or including measurements from glint for the retrieval of aerosol, surface and ocean parameters and at last on the remote sensing reflectance.

3.2.1. Impact of glint to the retrieval parameters

Figure 6 shows the Normalized Root Mean Square Error (NRMSE) defined as the RMSE between true and retrieved values of variable normalized by the standard deviation of true values.

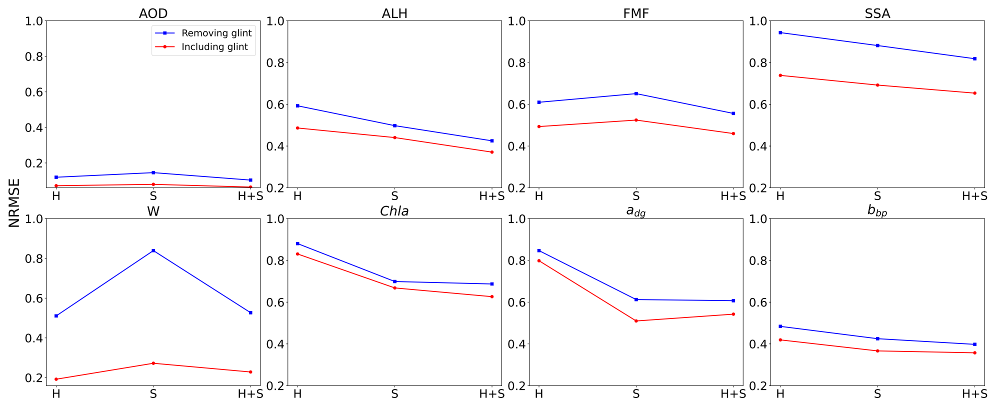

Fig. 6. NRMSE between retrieved vs true values of parameters from different configurations viz. HARP2-only (H), SPEXone-only (S), HARP2+SPEXone (H+S) with including or removing glint measurements. Y axis ranges from 0.2 to 1 for all subplots for better visual comparison.

$$\mathrm{NRMSE} = \frac{\sqrt{\frac{1}{n}\sum_{i=1}^{n}(y_i - \hat{y}_i)^2}}{\sqrt{\frac{1}{n}\sum_{i=1}^{n}(y_i - \bar{y})^2}} \tag{26}$$

Where, y_i, $\hat{y}_i$, $\bar{y}$ respectively denote true values, retrieved values and mean of true values. NRMSE provides normalized measure of retrieval error relative to the variability in the dataset. We chose metric NRMSE over RMSE and mean bias as it is independent of magnitude/unit of parameters being discussed. For all configurations, including measurements from glint shows the most significant improvement on wind speed and aerosol absorption. This is due to the fact that glint pattern is basically dependent on the magnitude of wind speed [79, 99] and the absorbing aerosols are easily recognized over the bright glint surface as has been shown in the studies [36, 40]. This indirectly improved FMF retrieval as the absorbing aerosols are present in the fine mode. The significant improvement in wind speed and SSA retrieval has also improved retrieval of other parameters indirectly. For example, better aerosol absorption retrieval improved the retrieval performance of ALH in the H configuration as ALH is sensitive to coupling between molecular scattering and aerosol absorption [100]. In the other two configurations (S and H+S) the spectral dependence becomes dominant. Glint measurements do not show significant impact in the retrieval performance of AOD. For the retrieval of ocean parameters, measurements in glint in addition to non-glint angles indirectly improve the performance by better characterizing the aerosol properties.

3.2.2. Performance evaluation of different configurations

Figure 6 shows that the UV sensitive parameters(e.g. a_{dg}, ALH, SSA) are retrieved significantly well from the S configuration compared to the H configuration. This is due to additional UV and near-UV wavelengths in the S configuration (385 ,400 , 410). Chla is also retrieved noticeably well with the S configuration compared to the H configuration due to the inclusion of more wavelengths in blue green range (470, 490, 510) in the S configuration which helped to account for its absorption features in blue and green range [101, 102]. Other aerosol parameters (AOD, FMF) have similar retrieval results from the S and H configurations. Wind speed is retrieved significantly better with the H configuration compared to the S configuration as the wide viewing angles in the H give advantage to retrieve wind governed surface reflection patterns. Furthermore, for all parameters except wind speed, the retrieval performance of the H+S configuration is better compared to the H configuration but is similar as compared to the S configuration. This observation shows that for aerosol retrieval (AOD, FMF) 5 viewing angles from the SPEXone instrument are sufficient and extra viewing angles from HARP2 add less information. This is consistent with the earlier sensitivity studies regarding number of viewing angles for aerosol retrieval [30, 37, 38]. Additional wavelengths in the UV and near-UV from SPEXone instrument are advantageous for the retrieval of UV sensitive parameters, and in blue green range are advantageous for the retrieval of Chla.

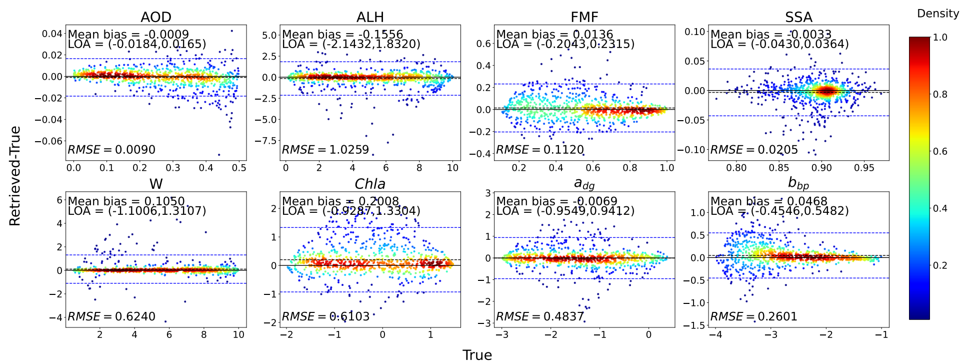

Fig. 7. Joint retrieval results from HARP2+SPEXone configuration (including glint). The black solid line is a line of equality with black dashed line indicating the mean bias. The blue dashed lines indicate the LOA.The ocean parameters Chla, a_{dg} and b_{bp} are in log scale.

Figure 7 shows the comparison of the retrieved and true values of aerosol, ocean and surface parameters from the HARP2+SPEXone configuration including the measurements from the glint region. As discussed earlier, this configuration has the advantage of having multi wavelengths range from UV to NIR and hence gives better retrieval for all parameters. The retrieval algorithm shows robust performance in retrieving aerosol optical depth (AOD) with almost zero mean bias and small RMSE of 0.009. The fine mode fraction (FMF) and aerosol layer height (ALH) are retrieved with a small mean bias of -0.15 km and 0.013 and RMSE of 1.02 km and 0.112 respectively. The SSA results obtained by using a post-processing NN with the retrieval parameters as inputs also show good agreement with true values with almost zero mean bias and RMSE of 0.02. As the measurements from glint are included which are highly influenced by wind speed, wind speed retrieval shows very good agreement with the mean bias and RMSE of 0.1 and 0.64 ms^{-1} respectively.Among the ocean parameters, Chla shows a mean bias of 0.2 with RMSE of 0.61, while the other parameters a_{dg} and b_{bp} have very small mean bias of -0.006 and 0.04 with RMSE of 0.48 and 0.26, respectively. It should be noted that, the retrieval results from inversion algorithms will be within the assumed boundary of parameters. When applying algorithm to real measurements, for cases out of the designed bounds the χ^2 value will be a good indicator of data quality.

These retrieval of aerosol optical parameters (For eg. AOD, SSA) compares well with existing state of the art algorithms. For example, AOD is retrieved with RMSE of 0.009 and with almost zero bias which is better than its retrieval from [29] (RMSE=0.03), [33] (RMSE=0.012), [32] (RMSE=0.011), [35] (RMSE 0.05). Similarly SSA is retrieved with RMSE of 0.02 which is better compared to its retrieval from [32] (RMSE=0.05), [29] (RMSE=0.04), [35] (RMSE=0.05). Note that the aerosol model used here has spectrally resolved refractive indices which is complex compared to the aerosol model in [25, 29, 32]. The retrieved aerosol layer height compares well with the existing algorithms [32, 48].

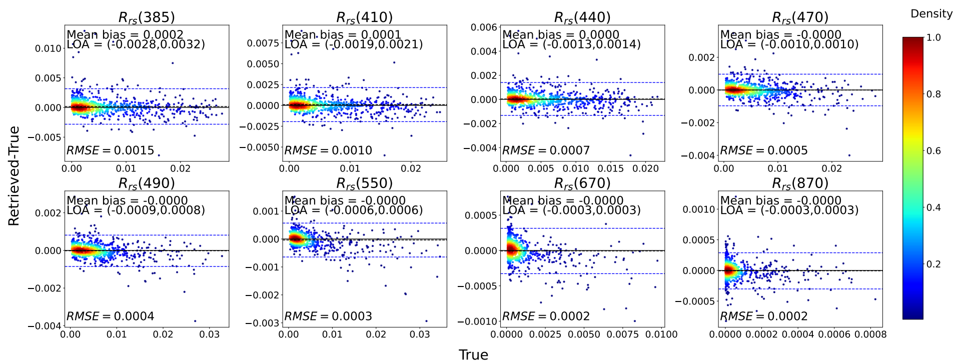

Fig. 8. Retrieval results for R_{rs} after atmospheric correction and BRDF correction. The black solid line is a line of equality with black dashed line indicating the mean bias and the blue dashed lines indicate the LOA.

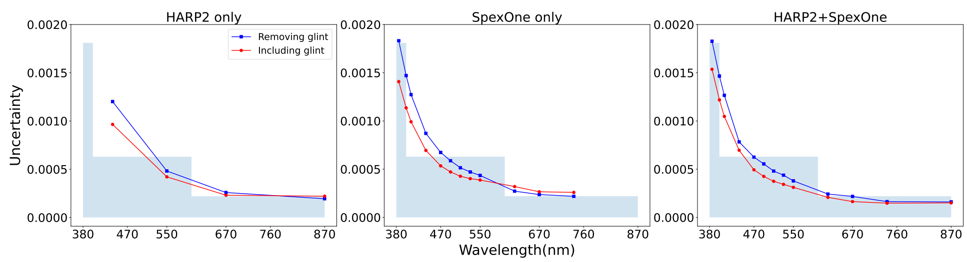

Fig. 9. R_{rs} uncertainties from different configurations. Shaded region indicates PACE uncertainty requirement for different wavelength ranges.

The retrieval of remote sensing reflectance R_{rs} is done via a post-processing procedure, in which the aerosol and ocean parameters from the joint retrieval algorithm are now used as an input to NN models for ρ_{a+s} and TBRDF. The atmospheric signal ρ_{a+s} and the transmittance included BRDF correction factors TBRDF are then incorporated in equation 17 to obtain remote sensing reflectance. During this process, we didn't add the additional measurement uncertainty to the simulated reflectance and hence the computed R_{rs} uncertainty is only due to the uncertainty in joint aerosol and ocean color retrieval. Fig 8 shows the errors in retrieved remote sensing reflectance plotted against their truth values. The truth R_{rs} was computed with a zenith sun and a nadir viewing direction. These results correspond to the H+S configuration with glint measurement included in the retrieval. Overall, the R_{rs} is retrieved well with zero mean bias at all wavelengths and RMSE less than 0.0006 for wavelengths 470-600, and equal to 0.0002 for wavelengths greater than 600 nm. Figure 9 summarizes the uncertainties of R_{rs} retrieval in terms of RMSE from different configurations with the shaded area indicating uncertainty requirements from PACE. The PACE uncertainty requirements [103] are 0.0018 or 20% for wavelengths 350-400 nm, 0.0006 or 5% for wavelengths 400-600 nm and 0.00022 or 10% for wavelengths 600-710 nm. These requirements levied on observations from the primary instrument on PACE, OCI, not the polarimeters, and they are expected to be met for at least 50% of the observable deep ocean (depth >1000m). It should be noted that [103] defined uncertainty requirements in terms of water leaving reflectance which are divided by π to obtain corresponding uncertainties in terms of remote sensing reflectance. For all configurations, addition of glint measurements reduced the R_{rs} uncertainty as it led to better atmospheric correction. The R_{rs} uncertainty for wavelengths 490 nm, 510 nm, 530 nm, 550nm are within PACE requirement with or without including glint measurements. For HARP2-only configuration, the uncertainty at 440 nm (RMSE=0.0012) is higher than that obtained from [29] (RMSE=0.0007) for open ocean while the uncertainties in other wavelengths are similar. Also, it should be noted that these uncertainties show strong AOD dependence with increased uncertainties for higher AOD [29,32]. The R_{rs} uncertainty improved for the H+S configuration with all bands meeting PACE threshold except for wavelengths 410 and 440 nm. Note that the PACE uncertainty limits are set for open ocean application not for complex coastal scenes.

4. Conclusion

In this study, we report the development of a joint retrieval algorithm, called FastMAPOL/component, for the MAP inversion of aerosol and ocean color information. The forward models are neural network models, which are trained to speed up the retrieval. The NN forward models can accurately predict polarimetric measurements with uncertainty much smaller than the measurement uncertainty of the instrument and hence are suitable to be used in operational joint retrieval algorithms. The FastMAPOL/component algorithm incorporates a multi-parameter bio-optical model and a component representation of aerosols which is suitable for coastal water environments. The forward models are trained at 13 different wavelengths from 385 to 870 nm, including all the HARP2 bands and a selection of the SPEXone bands. The retrieval algorithm has the capability to use measurements from different configurations of HARP2 and SPEXone. Using the simulated data from the radiative transfer model, we evaluated the retrieval performance of different configurations viz. HARP2-only, SPEXone-only, HARP2+SPEXone on aerosol, surface and ocean parameters. The retrieval results from synthetic measurements show that the UV measurements from SPEXone are highly valuable to improve the retrieval of UV sensitive parameters like a_{dg}, ALH and SSA. The Chla retrieval also benefits from additional bands in the blue-green range from SPEXone. For retrieval of the surface parameter (wind speed), the HARP2 configuration performs well due to its large range of viewing angles. Also, additional measurements from the glint signal contributed to a significant improvement in the retrieval of wind speed and the aerosol absorption parameter (SSA), which then indirectly helped improve retrieval of other parameters. Furthermore, the SPEXone-only configuration works equally well with the HARP2-only configuration for general aerosol and ocean color parameters except wind speed. The algorithm is augmented with modules for atmospheric correction and BRDF correction to obtain the remote sensing reflectance. The performance of all different configurations to obtain remote sensing reflectance is discussed. The results show that R_{rs} uncertainty for the joint retrieval algorithm in H+S configuration are within the PACE requirement, except for wavelengths 410 and 440 nm. These results using synthetic data validate robust performance of our joint retrieval algorithms even in coastal waters with complex aerosols in the atmosphere. The validation results with the real MAP measurements from the PACE mission will be included in the next part of study.

Funding. National Aeronautics and Space Administration (80NSSC20M0227).

Acknowledgments. The hardware used in the computational studies is part of the UMBC High Performance Computing Facility (HPCF). The facility is supported by the U.S. National Science Foundation through the MRI program (grant nos. CNS-0821258, CNS-1228778, and OAC-1726023) and the SCREMS program (grant no. DMS-0821311), with additional substantial support from the University of Maryland, Baltimore County (UMBC). See hpcf.umbc.edu for more information on HPCF and the projects using its resources.

Disclosures. The authors declare no conflicts of interest.

Data Availability Statement. Data underlying the results presented in this paper are not publicly available at this time but may be obtained from the authors upon reasonable request.

5. References

References

1. H. M. Dierssen and K. Randolph, “Remote sensing of ocean color,” in *Earth System Monitoring: Selected Entries from the Encyclopedia of Sustainability Science and Technology,* (Springer, 2012), pp. 439–472.
2. S. Levitus, J. I. Antonov, T. P. Boyer, and C. Stephens, “Warming of the world ocean,” Science **287**, 2225–2229 (2000).
3. R. Costanza, “The ecological, economic, and social importance of the oceans,” Ecol. economics **31**, 199–213 (1999).
4. S. E. Craig, C. T. Jones, W. K. Li, *et al.*, “Deriving optical metrics of coastal phytoplankton biomass from ocean colour,” Remote. Sens. Environ. **119**, 72–83 (2012).
5. T. Platt and S. Sathyendranath, “Oceanic primary production: estimation by remote sensing at local and regional scales,” Science **241**, 1613–1620 (1988).
6. S. Sathyendranath, T. Platt, C. M. Caverhill, *et al.*, “Remote sensing of oceanic primary production: computations using a spectral model,” Deep. Sea Res. Part A. Oceanogr. Res. Pap. **36**, 431–453 (1989).
7. M.-E. Carr, M. A. Friedrichs, M. Schmeltz, *et al.*, “A comparison of global estimates of marine primary production from ocean color,” Deep. Sea Res. Part II: Top. Stud. Oceanogr. **53**, 741–770 (2006).
8. D. Siegel, K. Buesseler, S. C. Doney, *et al.*, “Global assessment of ocean carbon export by combining satellite observations and food-web models,” Glob. Biogeochem. Cycles **28**, 181–196 (2014).
9. C. G. Fichot and R. Benner, “A novel method to estimate doc concentrations from cdom absorption coefficients in coastal waters,” Geophys. research letters **38** (2011).
10. U. Pöschl, “Atmospheric aerosols: composition, transformation, climate and health effects,” Angewandte Chemie Int. Ed. **44**, 7520–7540 (2005).
11. Y. Kaufman, D. Tanré, H. Gordon, *et al.*, “Passive remote sensing of tropospheric aerosol and atmospheric correction for the aerosol effect,” J. Geophys. Res. Atmospheres **102**, 16815–16830 (1997).
12. P.-Y. Deschamps, F.-M. Bréon, M. Leroy, *et al.*, “The polder mission: Instrument characteristics and scientific objectives,” IEEE Trans. on geoscience remote sensing **32**, 598–615 (1994).
13. D. J. Diner, F. Xu, M. J. Garay, *et al.*, “The airborne multiangle spectropolarimetric imager (airmspi): a new tool for aerosol and cloud remote sensing,” Atmospheric Meas. Tech. **6**, 2007–2025 (2013).
14. F. Snik, J. H. Rietjens, G. Van Harten, *et al.*, “Spex: the spectropolarimeter for planetary exploration,” in *Space Telescopes and Instrumentation 2010: Optical, Infrared, and Millimeter Wave,* vol. 7731 (SPIE, 2010), pp. 383–394.
15. B. Cairns, E. E. Russell, and L. D. Travis, “Research scanning polarimeter: calibration and ground-based measurements,” in *Polarization: measurement, analysis, and remote sensing II,* vol. 3754 (SPIE, 1999), pp. 186–196.
16. J. V. Martins, T. Nielsen, C. Fish, *et al.*, “Harp cubesat–an innovative hyperangular imaging polarimeter for earth science applications,” in *Small Sat Pre-Conference Workshop, Logan Utah,* vol. 20 (2014).
17. L. A. Remer, K. Knobelspiesse, P.-W. Zhai, *et al.*, “Retrieving aerosol characteristics from the pace mission, part 2: multi-angle and polarimetry,” Front. Environ. Sci. **7**, 94 (2019).
18. R. J. Frouin, B. A. Franz, A. Ibrahim, *et al.*, “Atmospheric correction of satellite ocean-color imagery during the pace era,” Front. Earth Sci. **7**, 145 (2019).
19. J. V. Martins, R. Fernandez-Borda, B. McBride, *et al.*, “The harp hype ran gular imaging polarimeter and the need for small satellite payloads with high science payoff for earth science remote sensing,” in *IGARSS 2018-2018 IEEE International Geoscience and Remote Sensing Symposium,* (IEEE, 2018), pp. 6304–6307.
20. O. P. Hasekamp, G. Fu, S. P. Rusli, *et al.*, “Aerosol measurements by spexone on the nasa pace mission: expected retrieval capabilities,” J. Quant. Spectrosc. Radiat. Transf. **227**, 170–184 (2019).
21. J. Rietjens, J. Campo, A. Chanumolu, *et al.*, “Expected performance and error analysis for spexone, a multi-angle channeled spectropolarimeter for the nasa pace mission,” in *Polarization Science and Remote Sensing IX,* vol. 11132 (SPIE, 2019), pp. 34–47.
22. J. Chowdhary, B. Cairns, M. I. Mishchenko, *et al.*, “Retrieval of aerosol scattering and absorption properties from photopolarimetric observations over the ocean during the clams experiment,” J. Atmospheric Sci. **62**, 1093–1117 (2005).
23. O. P. Hasekamp, P. Litvinov, and A. Butz, “Aerosol properties over the ocean from parasol multiangle photopolarimetric measurements,” J. Geophys. Res. Atmospheres **116** (2011).
24. F. Xu, O. Dubovik, P.-W. Zhai, *et al.*, “Joint retrieval of aerosol and water-leaving radiance from multispectral, multiangular and polarimetric measurements over ocean,” Atmospheric Meas. Tech. **9**, 2877–2907 (2016).
25. S. Stamnes, C. Hostetler, R. Ferrare, *et al.*, “Simultaneous polarimeter retrievals of microphysical aerosol and ocean color parameters from the “mapp” algorithm with comparison to high-spectral-resolution lidar aerosol and ocean products,” Appl. optics **57**, 2394–2413 (2018).
26. F. Xu, L. Gao, J. Redemann, *et al.*, “A combined lidar-polarimeter inversion approach for aerosol remote sensing over ocean,” Front. Remote. Sens. **2**, 620871 (2021).
27. C. D. Mobley, D. Stramski, W. Paul Bissett, and E. Boss, “Optical modeling of ocean waters: Is the case 1-case 2 classification still useful?” Oceanography **17**, 60 (2004).
28. M. Gao, P.-W. Zhai, B. Franz, *et al.*, “Retrieval of aerosol properties and water-leaving reflectance from multi-angular polarimetric measurements over coastal waters,” Opt. express **26**, 8968–8989 (2018).
29. M. Gao, B. A. Franz, K. Knobelspiesse, *et al.*, “Efficient multi-angle polarimetric inversion of aerosols and ocean

color powered by a deep neural network forward model," Atmospheric Meas. Tech. **14**, 4083–4110 (2021).
30. M. Gao, K. Knobelspiesse, B. A. Franz, *et al.*, "Adaptive data screening for multi-angle polarimetric aerosol and ocean color remote sensing accelerated by deep learning," Front. Remote. Sens. **2**, 757832 (2021).
31. M. Gao, K. Knobelspiesse, B. A. Franz, *et al.*, "Effective uncertainty quantification for multi-angle polarimetric aerosol remote sensing over ocean," Atmospheric Meas. Tech. **15**, 4859–4879 (2022).
32. M. Gao, B. A. Franz, P.-W. Zhai, *et al.*, "Simultaneous retrieval of aerosol and ocean properties from pace harp2 with uncertainty assessment using cascading neural network radiative transfer models," EGUsphere **2023**, 1–31 (2023).
33. S. Stamnes, M. Jones, J. G. Allen, *et al.*, "The pace-mapp algorithm: Simultaneous aerosol and ocean polarimeter products using coupled atmosphere-ocean vector radiative transfer," Front. Remote. Sens. **4**, 1174672 (2023).
34. L. Li, O. Dubovik, Y. Derimian, *et al.*, "Retrieval of aerosol components directly from satellite and ground-based measurements," Atmospheric Chem. Phys. **19**, 13409–13443 (2019).
35. C. Chen, O. Dubovik, D. Fuertes, *et al.*, "Validation of grasp algorithm product from polder/parasol data and assessment of multi-angular polarimetry potential for aerosol monitoring," Earth Syst. Sci. Data Discuss. **2020**, 1–108 (2020).
36. K. Knobelspiesse, A. Ibrahim, B. Franz, *et al.*, "Analysis of simultaneous aerosol and ocean glint retrieval using multi-angle observations," Atmospheric Meas. Tech. **14**, 3233–3252 (2021).
37. O. P. Hasekamp and J. Landgraf, "Retrieval of aerosol properties over land surfaces: capabilities of multiple-viewing-angle intensity and polarization measurements," Appl. optics **46**, 3332–3344 (2007).
38. L. Wu, O. Hasekamp, B. Van Diedenhoven, and B. Cairns, "Aerosol retrieval from multiangle, multispectral photopolarimetric measurements: importance of spectral range and angular resolution," Atmospheric Meas. Tech. **8**, 2625–2638 (2015).
39. F. Xu, G. Van Harten, D. J. Diner, *et al.*, "Coupled retrieval of aerosol properties and land surface reflection using the airborne multiangle spectropolarimetric imager," J. Geophys. Res. Atmospheres **122**, 7004–7026 (2017).
40. Y. Kaufman, J. Martins, L. Remer, *et al.*, "Satellite retrieval of aerosol absorption over the oceans using sunglint," Geophys. Res. Lett. **29**, 34–1 (2002).
41. P.-W. Zhai, Y. Hu, C. R. Trepte, and P. L. Lucker, "A vector radiative transfer model for coupled atmosphere and ocean systems based on successive order of scattering method," Opt. express **17**, 2057–2079 (2009).
42. P.-W. Zhai, Y. Hu, J. Chowdhary, *et al.*, "A vector radiative transfer model for coupled atmosphere and ocean systems with a rough interface," J. Quant. Spectrosc. Radiat. Transf. **111**, 1025–1040 (2010).
43. M. Chin, R. B. Rood, S.-J. Lin, *et al.*, "Atmospheric sulfur cycle simulated in the global model gocart: Model description and global properties," J. Geophys. Res. Atmospheres **105**, 24671–24687 (2000).
44. M. Hess, P. Koepke, and I. Schult, "Optical properties of aerosols and clouds: The software package opac," Bull. Am. meteorological society **79**, 831–844 (1998).
45. S. Gasso, D. Hegg, D. Covert, *et al.*, "Influence of humidity on the aerosol scattering coefficient and its effect on the upwelling radiance during ace-2," Tellus B: Chem. Phys. Meteorol. **52**, 546–567 (2000).
46. M. I. Mishchenko, L. D. Travis, and A. A. Lacis, *Scattering, absorption, and emission of light by small particles* (Cambridge university press, 2002).
47. Z. Meng, P. Yang, G. W. Kattawar, *et al.*, "Single-scattering properties of tri-axial ellipsoidal mineral dust aerosols: A database for application to radiative transfer calculations," J. Aerosol Sci. **41**, 501–512 (2010).
48. L. Wu, O. Hasekamp, B. van Diedenhoven, *et al.*, "Passive remote sensing of aerosol layer height using near-uv multiangle polarization measurements," Geophys. research letters **43**, 8783–8790 (2016).
49. J. Reid, R. Koppmann, T. Eck, and D. Eleuterio, "A review of biomass burning emissions part ii: intensive physical properties of biomass burning particles," Atmospheric chemistry physics **5**, 799–825 (2005).
50. P. Koepke, M. Hess, I. Schult, and E. P. Shettle, "Global aerosol data set," Tech. rep., Max-Planck-Institut für Meteorologie (1997).
51. Z. Ahmad, B. A. Franz, C. R. McClain, *et al.*, "New aerosol models for the retrieval of aerosol optical thickness and normalized water-leaving radiances from the seawifs and modis sensors over coastal regions and open oceans," Appl. optics **49**, 5545–5560 (2010).
52. M. Saito, P. Yang, J. Ding, and X. Liu, "A comprehensive database of the optical properties of irregular aerosol particles for radiative transfer simulations," J. Atmospheric Sci. **78**, 2089–2111 (2021).
53. T. C. Bond and R. W. Bergstrom, "Light absorption by carbonaceous particles: An investigative review," Aerosol science technology **40**, 27–67 (2006).
54. T. W. Kirchstetter, T. Novakov, and P. V. Hobbs, "Evidence that the spectral dependence of light absorption by aerosols is affected by organic carbon," J. Geophys. Res. Atmospheres **109** (2004).
55. G. Ghosh, "Dispersion-equation coefficients for the refractive index and birefringence of calcite and quartz crystals," Opt. communications **163**, 95–102 (1999).
56. C. Di Biagio, P. Formenti, Y. Balkanski, *et al.*, "Complex refractive indices and single-scattering albedo of global dust aerosols in the shortwave spectrum and relationship to size and iron content," Atmospheric Chem. Phys. **19**, 15503–15531 (2019).
57. A. Bricaud, A. Morel, M. Babin, *et al.*, "Variations of light absorption by suspended particles with chlorophyll a concentration in oceanic (case 1) waters: Analysis and implications for bio-optical models," J. Geophys. Res. Ocean. **103**, 31033–31044 (1998).
58. P. J. Werdell, B. A. Franz, S. W. Bailey, *et al.*, "Generalized ocean color inversion model for retrieving marine

inherent optical properties," Appl. optics **52**, 2019–2037 (2013).
59. Y. Huot, A. Morel, M. Twardowski, *et al.*, "Particle optical backscattering along a chlorophyll gradient in the upper layer of the eastern south pacific ocean," Biogeosciences **5**, 495–507 (2008).
60. N. K. Hannadige, P.-W. Zhai, P. J. Werdell, *et al.*, "Optimizing retrieval spaces of bio-optical models for remote sensing of ocean color," Appl. Opt. **62**, 3299–3309 (2023).
61. N. K. Hannadige, P.-W. Zhai, M. Gao, *et al.*, "Performance evaluation of three bio-optical models in aerosol and ocean color joint retrievals," Atmospheric Meas. Tech. Discuss. **2023**, 1–31 (2023).
62. L. Kou, D. Labrie, and P. Chylek, "Refractive indices of water and ice in the 0.65-to 2.5-μm spectral range," Appl. optics **32**, 3531–3540 (1993).
63. R. M. Pope and E. S. Fry, "Absorption spectrum (380–700 nm) of pure water. ii. integrating cavity measurements," Appl. optics **36**, 8710–8723 (1997).
64. X. Zhang, L. Hu, and M.-X. He, "Scattering by pure seawater: Effect of salinity," Opt. express **17**, 5698–5710 (2009).
65. A. MOREL, "Optical properties of pure water and pure sea water," Opt. Aspects Oceanogr. **1** (1974).
66. C. D. Mobley, B. Gentili, H. R. Gordon, *et al.*, "Comparison of numerical models for computing underwater light fields," Appl. Opt. **32**, 7484–7504 (1993).
67. G. R. Fournier and J. L. Forand, "Analytic phase function for ocean water," in *Ocean Optics XII,* vol. 2258 (SPIE, 1994), pp. 194–201.
68. J. M. Sullivan and M. S. Twardowski, "Angular shape of the oceanic particulate volume scattering function in the backward direction," Appl. Opt. **48**, 6811–6819 (2009).
69. K. J. Voss and E. S. Fry, "Measurement of the mueller matrix for ocean water," Appl. optics **23**, 4427–4439 (1984).
70. Z. Lee and K. L. Carder, "Effect of spectral band numbers on the retrieval of water column and bottom properties from ocean color data," Appl. Opt. **41**, 2191–2201 (2002).
71. Z. Lee, K. Carder, R. Arnone, and M. He, "Determination of primary spectral bands for remote sensing of aquatic environments," Sensors **7**, 3428–3441 (2007).
72. X. Chen, X. Xu, J. Wang, and D. J. Diner, "Can multi-angular polarimetric measurements in the oxygen-a and b bands improve the retrieval of aerosol vertical distribution?" J. Quant. Spectrosc. Radiat. Transf. **270**, 107679 (2021).
73. L. Mukherjee, P.-W. Zhai, M. Gao, *et al.*, "Neural network reflectance prediction model for both open ocean and coastal waters," Remote. Sens. **12**, 1421 (2020).
74. K. Aryal, P.-W. Zhai, M. Gao, and B. A. Franz, "Instantaneous photosynthetically available radiation models for ocean waters using neural networks," Appl. Opt. **61**, 9985–9995 (2022).
75. K. Aryal, P. Zhai, B. A. Franz, *et al.*, "Accurate brdf correction factor prediction model using neural network for ocean waters," in *AGU Fall Meeting Abstracts,* vol. 2022 (2022), pp. A52I–1079.
76. U. S. Atmosphere, *US standard atmosphere* (National Oceanic and Atmospheric Administration, 1976).
77. P. Zhai, M. Gao, B. A. Franz, *et al.*, "A radiative transfer simulator for pace: theory and applications," Front. Remote. Sens. p. 2 (2022a).
78. P.-W. Zhai and Y. Hu, "An improved pseudo spherical shell algorithm for vector radiative transfer," J. Quant. Spectrosc. Radiat. Transf. **282**, 108132 (2022b).
79. C. Cox and W. Munk, "Measurement of the roughness of the sea surface from photographs of the sun's glitter," Josa **44**, 838–850 (1954).
80. P. Koepke, "Effective reflectance of oceanic whitecaps," Appl. optics **23**, 1816–1824 (1984).
81. Z. Lee, "Models, parameters, and approaches that used to generate wide range of absorption and backscattering spectra," Ocean. Color. Algorithm Work. Group, IOCCG (2003).
82. Z. Lee, R. Arnone, C. Hu, *et al.*, "Uncertainties of optical parameters and their propagations in an analytical ocean color inversion algorithm," Appl. Opt. **49**, 369–381 (2010).
83. H. Loisel, D. S. F. Jorge, R. A. Reynolds, and D. Stramski, "A synthetic database generated by radiative transfer simulations in support of studies in ocean optics and optical remote sensing of the global ocean," Earth Syst. Sci. Data Discuss. **2023**, 1–24 (2023).
84. M. Defoin-Platel and M. Chami, "How ambiguous is the inverse problem of ocean color in coastal waters?" J. Geophys. Res. Ocean. **112** (2007).
85. A. Morel and B. Gentili, "Diffuse reflectance of oceanic waters. iii. implication of bidirectionality for the remote-sensing problem," Appl. optics **35**, 4850–4862 (1996).
86. C. D. Mobley, J. Werdell, B. Franz, *et al.*, "Atmospheric correction for satellite ocean color radiometry," Tech. rep., National Aeronautics and Space Administration (2016).
87. B. A. McBride, J. V. Martins, J. D. Cieslak, *et al.*, "Pre-launch calibration and validation of the airborne hyper-angular rainbow polarimeter (airharp) instrument," EGUsphere **2023**, 1–52 (2023).
88. D. P. Kingma and J. Ba, "Adam: A method for stochastic optimization," arXiv preprint arXiv:1412.6980 (2014).
89. I. Loshchilov and F. Hutter, "Decoupled weight decay regularization," arXiv preprint arXiv:1711.05101 (2017).
90. C. C. Aggarwal *et al.*, "Neural networks and deep learning," Springer **10**, 978–3 (2018).
91. C. D. Rodgers, *Inverse methods for atmospheric sounding: theory and practice*, vol. 2 (World scientific, 2000).
92. M. Gao, K. Knobelspiesse, B. A. Franz, *et al.*, "The impact and estimation of uncertainty correlation for multi-angle polarimetric remote sensing of aerosols and ocean color," Atmospheric Meas. Tech. **16**, 2067–2087 (2023).
93. R. Gelaro, W. McCarty, M. J. Suárez, *et al.*, "The modern-era retrospective analysis for research and applications, version 2 (merra-2)," J. climate **30**, 5419–5454 (2017).

94. M. A. Branch, T. F. Coleman, and Y. Li, "A subspace, interior, and conjugate gradient method for large-scale bound-constrained minimization problems," SIAM J. on Sci. Comput. **21**, 1–23 (1999).
95. A. G. Baydin, B. A. Pearlmutter, A. A. Radul, and J. M. Siskind, "Automatic differentiation in machine learning: a survey," J. Marchine Learn. Res. **18**, 1–43 (2018).
96. J. M. Bland and D. Altman, "Statistical methods for assessing agreement between two methods of clinical measurement," The lancet **327**, 307–310 (1986).
97. S. Maritorena, D. A. Siegel, and A. R. Peterson, "Optimization of a semianalytical ocean color model for global-scale applications," Appl. optics **41**, 2705–2714 (2002).
98. Z. K. Erickson, L. McKinna, P. J. Werdell, and I. Cetinić, "Bayesian approach to a generalized inherent optical property model," Opt. Express **31**, 22790–22801 (2023).
99. T. Harmel and M. Chami, "Determination of sea surface wind speed using the polarimetric and multidirectional properties of satellite measurements in visible bands," Geophys. Res. Lett. **39** (2012).
100. L. Duforêt, R. Frouin, and P. Dubuisson, "Importance and estimation of aerosol vertical structure in satellite ocean-color remote sensing," Appl. optics **46**, 1107–1119 (2007).
101. H. M. Dierssen, "Perspectives on empirical approaches for ocean color remote sensing of chlorophyll in a changing climate," Proc. National Acad. Sci. **107**, 17073–17078 (2010).
102. C. Hu, Z. Lee, and B. Franz, "Chlorophyll aalgorithms for oligotrophic oceans: A novel approach based on three-band reflectance difference," J. Geophys. Res. Ocean. **117** (2012).
103. P. J. Werdell, M. J. Behrenfeld, P. S. Bontempi, *et al.*, "The plankton, aerosol, cloud, ocean ecosystem mission: status, science, advances," Bull. Am. Meteorol. Soc. **100**, 1775–1794 (2019).